RSC Advances

REVIEW

View Article Online
View Journal | View Issue

Cite this: *RSC Adv.*, 2025, **15**, 45112

In-fiber composite nanostructures formed through filamentation instability during the thermal drawing process

Peihao Li, Hui Deng, Weixue Xia, Qingchang Meng, Wenbin Yi, Yue Ben and Bingrui Xu *

Long and flexible fibers with composite nanostructures have impactful applications in sensing, energy harvesting, biomedicine, and healthcare. Recent progress on in-fiber nanostructures from the perspective of filamentation instability is reviewed. The physical mechanism of filamentation instability is revealed by considering both the stretching effect and van der Waals forces, and theoretical predictions reach a close agreement with experimental results. Then, it is shown that using textured films in the preform with varying template thickness, the filamentation instability can be controlled to obtain a prescribed diameter and periodicity of ordered nanowire arrays in fibers. The filamentation instability of multilayer sheets has been investigated to get fibers with multilayer and multimaterial nanostructures. Lastly, second-order nonlinear stability analysis could provide guidance on the diameters of the main nanowires and satellite nanowires in fibers. This review could motivate more work in the future to obtain various multifunctional and multimaterial fibers through filamentation instability.

Received 21st August 2025
Accepted 16th October 2025

DOI: 10.1039/d5ra06202k

rsc.li/rsc-advances

1 Introduction

During the thermal drawing process, a preform is heated into a viscous fluid state and then stretched into long fibers, which is a proven technology to produce kilometer-long optical fibers in the telecommunications industry. Over the past twenty years, this technology has been successfully employed to fabricate advanced multimaterial fibers and textiles.[1–4] Typically, the structure and geometric configuration of the cross section in the preform are well preserved in the final fiber, with only a proportional reduction in terms of dimensions (multilayer cylindrical sheets,[5–12] or multilayer planar sheets[13–16]), since the flow instability is suppressed by the high viscosity of the materials during the thermal drawing process. These designed fibers are composed of distinctive materials and complex geometries, enabling sophisticated integrated functionalities for extensive applications in optoelectronics, energy harvesting, sensing, biomedicine, and healthcare.[1–4] The radial dependency of the axial velocity,[17] cracks and deformations of semiconducting cores,[18] and thermal shrinkage behavior and thermo-mechanical properties[19] have been investigated for

Department of Basic Courses, Naval Engineering University, Wuhan, 430033, China. E-mail: brxu@fudan.edu.cn

Peihao Li

Bingrui Xu

deeper insight into multimaterial fiber formation during thermal drawing and better fabrication of advanced functional fibers.

Flow instabilities are ubiquitous in nature, with different patterns and many engineering applications.[20,21] For example, liquid threads break up into droplets in ink-jet printing, the wine-tear phenomenon arises from capillary ridge instability, and viscous coiling instability happens when highly viscous fluids fall on a solid surface. Recently, fluid instabilities have been employed during thermal drawing to further extend the fabrication of micro/nano-structures in fibers and textiles.[22–24]

There are mainly two instability phenomena during the thermal drawing process. Firstly, capillary instability has been fruitfully employed in post-drawing processes to obtain particles with various structures (multishell particles, multicomponent particles, composite particles, porous particles, *etc.*) and fibers with embedded particle assemblies (from 1D to 3D assemblies).[25–28] Theoretical models including nonlinear effects have been implemented to better understand the fundamentals of the in-fiber capillary instability, especially particle size selection and prediction.[18,29,30] These particle-based multifunctional fibers have potential applications in optoelectronics, micro/nano-technologies, and biomedicine.[22–24]

The other phenomenon is the filamentation instability in multi-layer sheets when viscous sheets are further stretched to the nanoscale.[23,31,32] When a sandwiched As_2Se_3 sheet is stretched as thin as 10 nm in a PES/As_2Se_3/PES structure, it is observed that the As_2Se_3 sheet breaks up into a set of continuous filaments, *i.e.*, the filamentation instability phenomenon.[23,31] The instability and rupture of liquid viscous sheets have been investigated experimentally and theoretically since the 1950s,[33–38] and Oron *et al.*[39] and Craster & Matar[40] reviewed works on the instability of thin viscous sheets over many decades. However, filamentation instability is significantly different from the common instability and breakup of liquid sheets, where instability occurs only in the perpendicular direction (perpendicular to the stretching direction) rather than in the parallel direction (along the stretching direction). The mechanism of filamentation instability is also revealed by combining van der Waals forces and the stretching effect, and its theoretical predictions are in close agreement with experimental results from 2019.[41] In-depth understanding of the filamentation instability has unlocked the ability to control and self-assemble filaments in fibers.[42–44] This intriguing filamentation phenomenon during the thermal drawing process opens new opportunities to fabricate nanowires and multifunctional fibers with micro/nanostructures.[41–46]

Besides the aforementioned capillary and filamentation instabilities, mechanical instability during planar fiber cold-drawing has also emerged as a pivotal complementary strategy for fabricating in-fiber nanostructures. For instance, a thin capping layer can act as a "mechanical buffer" to suppress premature fracture of 2D films during the elastic deformation stage of the polymer substrate.[47] Thermoplastic polymers subjected to a continuous tensile stress experience a state of mechanical instability, resulting in neck formation and propagation.[48] The necking process with strong localized strain enables the transformation of initially brittle polymeric materials into robust, flexible, and oriented forms.[49]

In this review, we mainly focus on in-fiber composite nanostructures from the perspective of filamentation instability. Firstly, the physical mechanism of filamentation instability is reviewed.[41] Then, it is shown that using textured films in the preform with varying template thickness, the filamentation instability can be controlled to obtain a prescribed diameter and periodicity of ordered nanowire arrays in fibers.[43] The filamentation instability of multilayer sheets has been investigated to get fibers with multilayer and multimaterial nanostructures.[42] Lastly, second-order nonlinear stability analysis could provide guidance on the diameters of the main nanowires and satellite nanowires in fibers.[44]

2 Physical mechanism of filamentation instability

A liquid viscous sheet ruptures into an array of continuous filaments when the sheet thickness is further reduced to the nanoscale during the thermal drawing process. The Reynolds number in the filamentation phenomenon is found to be much less than 1, *i.e.* $\mathrm{Re} \ll 1$.[31,32] Thus, the capillary instability caused by aerodynamic forces for planar viscous sheets is irrelevant, with the relative motion between sheets and surrounding fluids playing an important role.[35] Therefore, another destabilizing factor should be introduced to explain the observed filamentation instability. It is noted that the thickness of thin liquid sheets is thinned down to the nanoscale when the filamentation phenomenon happens. This brings to mind the spinodal dewetting phenomenon for sheets with a thickness less than 1 μm, dominated by the long-range behavior of van der Waals forces.[50]

Moreover, in filamentation instability, ruptures appear purely in the perpendicular direction rather than in the parallel direction, as shown in Fig. 1a. Therefore, this filamentation instability phenomenon can be termed 'anisotropic instability of a stretching viscous sheet' (AISVS). In the AISVS phenomenon, besides van der Waals forces dominating the instability as mentioned above, the stretching effect should be taken into account, similar to a viscous thread falling under gravity where the instability is suppressed and capillary breakup is delayed.[51] Thus, the physical mechanism of the AISVS phenomenon is suggested by considering both van der Waals forces and the stretching effect, as shown in Fig. 1b: (I) a viscous sheet is stretched – the perpendicular and parallel directions are marked; (II) perturbations in the perpendicular direction dramatically grow, but perturbations in the parallel direction are suppressed; (III) perturbations keep growing over time; (IV) consequently, the viscous sheet ruptures into an array of filaments.[41]

2.1 Linear stability analysis

In the mathematical model, a viscous thin sheet (viscosity μ_1) with initial thickness H_0, velocity w_0, and initial width $2\ell_0$, sandwiched by another fluid (viscosity μ_2), is stretched over

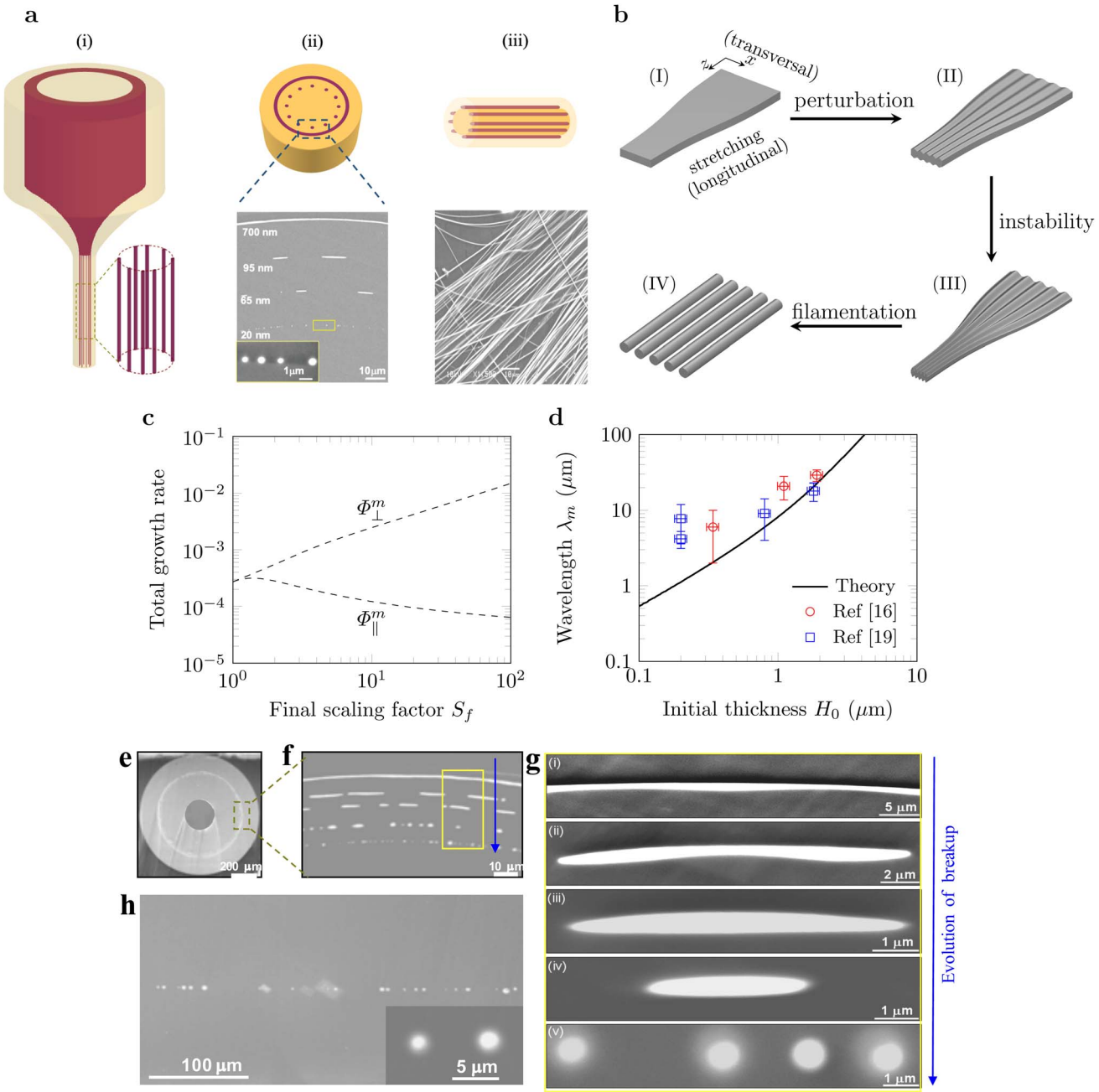

Fig. 1 The filamentation phenomenon. (a) Filamentation instability during the thermal drawing process: (i) sketch; (ii) rupture of the liquid sheet in the perpendicular direction; (iii) continuous filaments in the parallel direction. Reprinted (adapted) with permission,[31] copyright (2008) American Chemical Society. (b) Mechanism sketch for AISVS. (c) Maximum total growth rates $\Phi_\parallel^m$ in the parallel direction and $\Phi_\perp^m$ in the perpendicular direction. (d) In the PSU/Se/PSU structure, the prediction of the breakup wavelength reaches a close agreement with the wavelength measured from experiments. (e–h) SEM images of the filamentation instability in the perpendicular direction. (b–h) Reprinted with permission,[41] copyright (2019) by the American Physical Society.

a length L to the take-up speed w_f. For this sheet, the thinning thickness rate is $S_H = H_0/H$, and the width thinning rate is $S_\ell = \ell_0/\ell$. The length of fluid elements along the parallel direction extends at a rate of $S_H S_\ell$ due to flow continuity. Therefore, the wavenumbers of perturbations in the parallel direction $k_\parallel$ and in the perpendicular direction $k_\perp$, the flow velocity w and the thickness of the stretching sheet H are associated with[41]

$$k_\parallel S_H S_\ell = \text{const}, \quad k_\perp / S_\ell = \text{const}, \quad w/S_H S_\ell = w_0, \quad HS_H = \text{const}. \tag{1}$$

According to the linear stability analysis of uniform planar sheets in another viscous fluid dominated by van der Waals forces,[41,52] the perturbation growth rate is expressed:

$$\omega(k,H) = -\frac{\gamma_{\text{eff}}k}{2}$$

$$\frac{\mu_2(\cosh(kH)-1)+\mu_1(\sinh(kH)-kH)}{\mu_2{}^2(\sinh(kH)+kH)+2\mu_1\mu_2\cosh(kH)+\mu_1{}^2(\sinh(kH)-kH)}. \quad (2)$$

Here the term of the van der Waals forces appears in the effective surface tension $\gamma_{\text{eff}} = \gamma - \text{A}/(k^2\pi H^4)$, with the surface tension γ and the Hamaker number A between two fluids.[41]

In the presence of the stretching effect, perturbations along the perpendicular direction grow dramatically compared to ones along the parallel direction (*i.e.*, the instability development). To quantitatively estimate the evolution of perturbations in both directions, the total growth rate integrating the local growth rate $\omega(k,H)$ could be constructive.[41,51] For perturbations introduced at position z_p, the total growth rate in the perpendicular direction ($\Phi_\perp$) as well as the one in the parallel stretching direction ($\Phi_\parallel$) can be determined:[41]

$$\Phi_\parallel(z_\text{p},k_\parallel) = \int_{t_p}^{t} \omega_\parallel[k_\parallel(\tau),H(\tau)]\,\text{d}\tau$$
$$= \int_{z_\text{p}}^{L} \frac{1}{w_0 S_\ell(\zeta)S_H(\zeta)}\omega_\parallel\left[k_\parallel(z_\text{p})\frac{S_H(z_\text{p})S_\ell(z_\text{p})}{S_H(\zeta)S_\ell(\zeta)}, H(z_\text{p})\frac{S_H(z_\text{p})}{S_H(\zeta)}\right]\text{d}\zeta, \quad (3a)$$

$$\Phi_\perp(z_\text{p},k_\perp) = \int_{t_\text{p}}^{t} \omega_\perp[k_\perp(\tau),H(\tau)]\text{d}\tau$$
$$= \int_{z_\text{p}}^{L} \frac{1}{w_0 S_\ell(\zeta)S_H(\zeta)}\omega_\perp\left[k_\perp(z_\text{p})\frac{S_\ell(\zeta)}{S_\ell(z_\text{p})}, H(z_\text{p})\frac{S_H(z_p)}{S_H(\zeta)}\right]\text{d}\zeta. \quad (3b)$$

Here, the integral on time is converted into an integral on space by substituting the local velocity expression $\text{d}\tau = \text{d}\zeta/(w_0 S_\ell S_H)$. The maximum total growth rates in the parallel direction $\Phi_\parallel^\text{m} = \max[\Phi_\parallel(z_\text{p},k_\parallel)]$ and in the perpendicular direction $\Phi_\perp^\text{m} = \max[\Phi_\perp(z_\text{p},k_\perp)]$ should dominate the instability.[41]

At first, perturbations brought in at the starting point $z_\text{p} = 0$ in the 'fiber limit' case are considered, where the thinning rates of thickness and width are equal $S_H = S_\ell$ and the final thinning factor S_f is defined as the thinning rate at $z = L$, *i.e.*, $S_\text{f} = S_H(L) = S_\ell(L)$.[41] In Fig. 1c, the maximum total growth rates in the parallel direction ($\Phi_\parallel^\text{m}$) and in the perpendicular direction ($\Phi_\perp^\text{m}$) *versus* the final thinning factor S_f are presented. When there is no stretching ($S_\text{f} = 1$), perturbations along both directions grow equally with $\Phi_\parallel^\text{m} = \Phi_\perp^\text{m}$. In the presence of stretching ($S_\text{f} > 1$), the stretching effect dramatically enhances the perpendicular instability but suppresses the parallel instability, $\Phi_\parallel^\text{m} < \Phi_\perp^\text{m}$. Similar results can be obtained for perturbations introduced at other positions. Therefore, the AISVS phenomenon (filamentation instability) appears and becomes more striking with increasing S_f.[41]

2.2 Comparison between theoretical predictions and experimental results

In a polysulfone (PSU)/Se/PSU structure with different initial thicknesses H_0 and perturbations brought in at any point $z_\text{p} \in (0, L)$, the maximum growth rates $\Phi_\perp^\text{m}$ are calculated. The most severe perturbation corresponding to the maximum growth rate $\Phi_\perp^\text{m}$ is introduced at z_m, and its initial wavenumber at z_m is $k_\perp^\text{m}$. Then the final theoretical breakup wavelength at $z = L$ can be worked out from $\lambda_\text{m} = 2\pi S(z_\text{m})/(k_\perp^\text{m} S_\text{f})$.[41]

During thermal drawing, the structures in the cross section are solidified in the fiber, so that it is possible to visualize the perpendicular instability through SEM (Fig. 1e–h). The wavelength in experiments (λ_exp) can be measured as the average space between filaments in SEM images of cross sections in fibers. The theoretical predictions reach a close agreement with experimental results,[31,41] as shown in Fig. 1d.

Filaments of semiconducting or other materials can be produced at the nanoscale, driven by filamentation instability during thermal drawing, creating fascinating possibilities in the manufacturing of nanowires on a large scale. It is noted that the diameter of the filaments and the space between the filaments are dominated by the most severe perturbation with the fastest total growth rate $\Phi_\perp^\text{m}$.

3 Controlled filamentation instability

For filamentation instability dominated by the maximum total growth rate $\Phi_\perp^\text{m}$, the diameter of the filaments and the space between the filaments are determined by the initial sheet thickness H_0 and the thinning factor S_f. Many practical applications in engineering have higher-level requirements; for example, a smaller space between filaments in fibers allows collective interaction and interference effects. Thus, precise control of filamentation instability can provide the preferred filament diameter space between filaments, key to advanced photonic and other applications.

The precise control of filamentation instability is realized using textured films in the preform with varying template thickness, as shown in Fig. 2a.[43] (1) A microscopic pattern with a periodic square is imprinted on a thermoplastic polymer with a polydimethylsiloxane (PDMS) stamp. (2) Then, the thermoplastic polymer film is reflowed to smooth out the pattern.[53] (3) A chalcogenide As_2Se_3 (or Se) is thermally evaporated onto the polymer substrate at an angle, resulting in a thickness fluctuation. (4) The films are encapsulated into a preform by hot-embossing another polymer film on top. (5) The preform is thermally drawn to microscopic dimensions, and the chalcogenide sheet breaks up into long nanowires (filaments) encapsulated in long flexible fibers, as shown in Fig. 2b and c. As presented in Fig. 2d and e, the filamentation instability can be manipulated by choosing an appropriate thickness and period of the deposited chalcogenide sheet to tune the nanowires with the desired diameter and spacing.[43]

The template thickness fluctuation can be assumed as a combination of varicose and sinuous perturbations with the preferred wavelength and initial amplitude (termed 'template perturbation'). It is anticipated that the template perturbation should dominate the filamentation instability instead of perturbation, with the fastest growth rate as the fiber is scaled down, so that the polymer film thins and ruptures at prescribed locations. This requires (1) the template perturbation to grow,

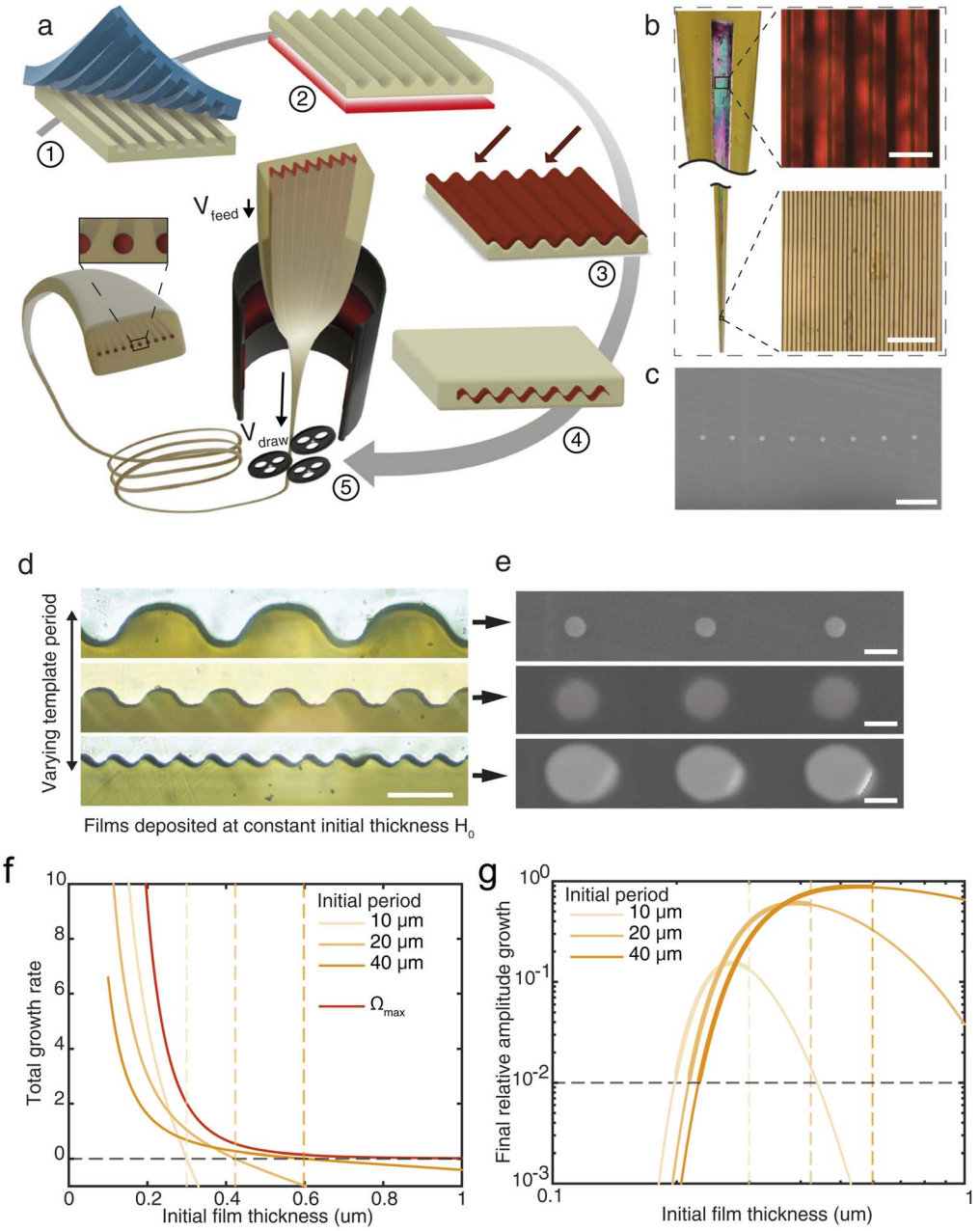

Fig. 2 Controlled nanowire-array fabrication process. (a) (1) A microscopic square pattern with a period is imprinted on a thermoplastic polymer with a PDMS stamp. (2) The polymer film is then reflowed to smooth out the pattern. (3) A chalcogenide As_2Se_3 (or Se) is thermally evaporated onto the polymer substrate at an angle, resulting in a thickness fluctuation. (4) The films are encapsulated into a preform by hot-embossing another polymer film on top. (5) The preform is thermally drawn to microscopic dimensions by adjusting the furnace temperature, and drawing and feeding speeds. The film breaks up periodically into long-ordered nanowires. (b) During thermal drawing, the continuous film in the preform (top) is heated and stretched, is subjected to fluid instability, and subsequently produces well-ordered filament arrays (bottom). (c) SEM cross-section of a thermally drawn fiber, demonstrating the perpendicular breakup. (d) Optical micrographs of cross-sections of the chalcogenide films after deposition onto a polymer substrate with different template periods. (e) SEM pictures of the corresponding nanowire array geometry. (f) Linearized model of the total instability growth rates during thermal drawing at three experimental template periodicities (termed the "initial period") and for the fastest-growing perturbation, for varying deposition thicknesses. Vertical dashed lines show the maximum thickness for which growth rates remain positive (horizontal dashed line). (g) Relative amplitude growth for varying film thicknesses. The horizontal dashed line shows the limit above which the template instability remains 100 times larger than the fastest growing one. Using vertical dashed lines from (d), a range of thicknesses for regular filament formation is estimated for each of the three cases (sections in bold). Figures reprinted with permission from ref. 43. Copyright (2022) by Springer Nature.

i.e., its total growth rate $\Phi_T > 0$, and (2) the final amplitude of template perturbation a_T to remain larger than that of the fastest-growing perturbation a_{max} throughout the drawing region:[43]

$$\frac{a_T}{a_{max}} = \frac{a_{T,0}}{a_{max,0}} \exp\left[(\Phi_T - \Phi_{max})t_f\right] > 1. \quad (4)$$

Here $a_{T,0}$ and $a_{max,0}$ are the initial amplitudes at $t = 0$ of the template perturbation and fastest-growing perturbation, and t_f is the stretching time in the drawing region. For a typical textured film $a_{T,0}/a_{max,0} = 100$; thus, the relative amplitude growth $\exp[(\Phi_T - \Phi_{max})t_f] > 0.01$.

In Fig. 2f, the total growth rates of three experimental template perturbations and the fastest-growing perturbations during thermal drawing are plotted, and dashed lines give the maximum thicknesses required for $\Phi_T > 0$. The relative amplitude growth $\exp[(\Phi_T - \Phi_{max})t_f]$ for varying film thicknesses is shown in Fig. 2g, and the amplitude growth of the template perturbation is 100 times larger than that of the fastest-growing perturbation above the horizontal dashed line. With the vertical dashed lines obtained from Fig. 2f, the thickness range for controlled filamentation is estimated for the three cases with different initial periods (sections in bold). Besides the linear analysis, fully numerical modelling has also been also performed, and the evolution of the instability also validates the rationale of controlled filamentation instability by textured films in the preform.[43]

Fabricating nanowires with the desired diameter and spacing in the fibers through controlled filamentation instability allows tuning of diffraction efficiencies.[43] Moreover, it is possible to obtain self-assembly metasurfaces in multimaterial fibers during the thermal drawing process. This process with massive production opens up a route to fabricate ultralong tunable nanowires and flexible fibers with embedded nanowire assemblies for nanophotonics and optoelectronic applications.[43]

4 Multilayer composite nanostructures

Many practical applications in photonics require fibers with multilayer and multimaterial structures,[14,17,19,27,43] and filamentation instability in multilayer sheets during thermal drawing is necessary. A linear stability analysis has been performed for 2D multi-fluid sheets, as shown in Fig. 3a. The outermost layers (the 1st layer and the Nth layer) can be assumed to extend to infinity since they are much thicker than the sandwiched thin sheets. The dispersion relation between the perturbation wavenumber k and its growth rate ω is derived:[42]

$$\boldsymbol{A}_2(k) \times \boldsymbol{C} = \sigma \boldsymbol{A}_1(k) \times \boldsymbol{C}, \quad (5)$$

where $\boldsymbol{A}_2(k)$ and $\boldsymbol{A}_1(k)$ are matrices calculated from the geometry and fluid parameters, and the growth rate is the real part of the eigenvalue σ, *i.e.* $\omega = \mathrm{Re}(\sigma)$. This is a generalized eigenvalue problem, which is worked out with numerical methods.

There are $N - 1$ roots $\sigma_n(k)$ ($n = 1, 2, \ldots, N - 1$) for the generalized eigenvalue problem (5), and then the initial perturbation amplitudes $\varepsilon^{(i)}$ on the ith interface can be solved for each root $\sigma_n(k)$. The initial perturbation amplitudes on all interfaces $\boldsymbol{\varepsilon}_n = [\varepsilon_n^{(1)}, \varepsilon_n^{(2)}, \ldots, \varepsilon_n^{(N-1)}]$ (ε_n is normalized to $\|\varepsilon_n\| = 1$) are the 'eigen-amplitudes' corresponding to the root $\sigma_n(k)$.[52] Once the growth rate $\omega_n = \mathrm{Re}(\sigma_n) > 0$, this mode is unstable. For a wavenumber k, there are $(N - 1)$ solutions of growth rates for an N-layer problem. In Fig. 3b, the most unstable mode with the maximum value $\omega_m = \max_{n,k}(\omega_n(k))$ should dominate the instability of N-layer sheets, with its corresponding wavenumber k_m and eigen-amplitudes $\varepsilon_m = (\varepsilon_m^{(1)}, \varepsilon_m^{(2)}, \ldots, \varepsilon_m^{(N-1)})$.[42]

The four-layer $N = 4$ case with different viscosities, interfacial tensions, thicknesses, and so on, has been carefully studied.[42] It has been found that there are several different unstable modes, and the eigen-amplitudes corresponding to the maximum growth rate Ω_m can switch among various modes. For example, as shown in Fig. 3c, as the thickness ratio H_3/H_2 increases, the most unstable mode switches from mode A (varicose mode between the 1st and 3rd interfaces) to mode F (varicose mode between the 1st and 2nd interfaces). In mode A, the maximum growth rate Ω_m decreases with increasing thickness ratio H_3/H_2, but it increases in mode F.

These results of the filamentation instability in multilayer sheets are helpful in the design of composite nanostructures in fibers by manipulating this instability through multilayer structures and their thicknesses, as listed in Table 1.[42]

Firstly, to enhance the filamentation instability of highly viscous materials, appropriately designing the multilayer structure could increase the perturbation growth rate. For example, in Table 1, for the 3-layer PES/As_2Se_3/PES structure, the maximum growth rate $\omega_m = 1.33 \times 10^{-3}$ s^{-1} for a 50 nm As_2Se_3 sheet. Changing the 3-layer structure to the 4-layer PES/As_2Se_3/Se/PES structure with an additional Se layer with $H_{As_2Se_3} = H_{Se} = 50$ nm, the growth rate can be enhanced by almost one thousand times to $\omega_m = 0.952$ s^{-1}. It is noted that this growth rate is much larger than that in the 3-layer PES/As_2Se_3/Se structure with Se as a surrounding fluid. Thus, to accelerate the rupture of highly viscous materials, it is better to design an extra cladding layer of less viscous fluid with thickness $H_3 \approx H_2$ rather than simply setting this less viscous fluid as the surrounding fluid.

Secondly, to preserve the structure in the preform when using less viscous materials and to realize the fabrication of long fibers with in-fiber structures including such materials, it is necessary to reduce the perturbation growth rate. In Table 1, for the 4-layer PSU/Se/As_2Se_3/PSU structure with $H_{As_2Se_3} = H_{Se} = 30$ nm, the growth rate is still very large, *i.e.*, $\omega_m = 5.557$ s^{-1} (the less viscous Se layer dominates the instability and ruptures). To further restrain the filamentation instability, increasing the Se layer thickness to $H_{Se} = H_{cr} \times 30$ nm switches the dominating mode to the 'para-varicose' mode for the 3-layer structure with the high-viscosity As_2Se_3 layer, with a much slower growth rate of $\omega_m = 0.0191$ s^{-1}, as shown in Table 1.

Moreover, a layer of certain thickness can be assumed as the surrounding fluid for thin sheets in the vicinity, as shown in Fig. 3c; the dominating instability mode switches from mode A to

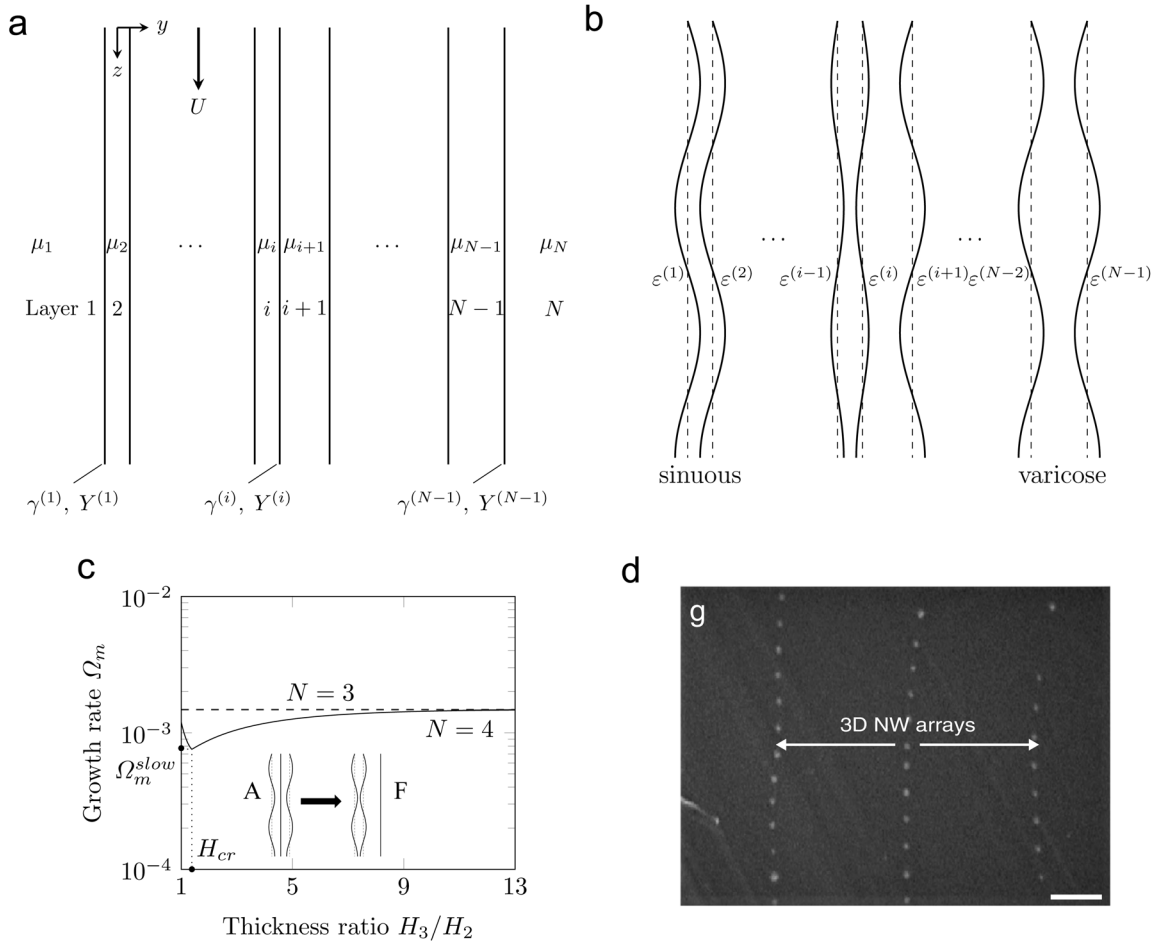

Fig. 3 Sketch of multilayer planar sheets: (a) N-layer liquid sheets with viscosities μ_i and $N-1$ interfaces $Y^{(i)}$ with interfacial tensions $\gamma^{(i)}$; (b) N-layer sheets with small perturbations in the linear stability analysis. (c) Maximum growth rates Ω_m at different cladding layer thicknesses H_3/H_2 for a four-layer ($N = 4$) problem (solid line), the corresponding three-layer limit ($N = 3$, $\eta_1 = 10$, $\eta_3 = 1$, dashed line), and the slowest growth rate Ω_m^{slow} accompanied with the critical thickness H_{cr}. Figures reprinted with permission,[42] copyright (2020) by the American Physical Society. (d) 3D self-assembled nanowire arrays in fibers from (g) in ref. 43. Figure reprinted with permission,[43] copyright (2022) by Springer Nature.

Table 1 Manipulating instability (perturbation growth rates) through designing multilayer structures and their thicknesses. Reprinted with permission,[42] copyright (2020) by the American Physical Society

Structure	Viscosities (Pa s)	Thicknesses (nm)	Growth rate ω_m (s^{-1})
PES/As_2Se_3/PES	$10^5/10^5/10^5$	$\infty/10/\infty$	0.703
PSU/Se/PSU	$10^5/1/10^5$	$\infty/80/\infty$	0.184
PES/As_2Se_3/PES	$10^5/10^5/10^5$	$\infty/50/\infty$	1.33×10^{-3}
PES/As_2Se_3/Se	$10^5/10^5/1$	$\infty/50/\infty$	2.56×10^{-3}
PES/As_2Se_3/Se/PES	$10^5/10^5/1/10^5$	$\infty/50/50/\infty$	0.952
PSU/Se/As_2Se_3/PSU	$10^5/1/10^5/10^5$	$\infty/30/30/\infty$	5.557
PSU/Se/As_2Se_3/PSU	$10^5/1/10^5/10^5$	$\infty/30H_{cr}/30/\infty$	0.0191
Se/As_2Se_3/PSU	$1/10^5/10^5$	$\infty/30/\infty$	0.0191

mode F with an increasing thickness ratio H_3/H_2. Consequently, this thick sheet layer can be utilized as a detached layer, diminishing the interaction and influence between adjacent layers. Therefore, a multilayer structure can be divided into combinations of multiple 3-layer, 4-layer or 5-layer sub-structures to attain highly integrated in-fiber composite nanostructures through a single thermal drawing process, such as the self-assembled 3D nanowire structure in the fibers in Fig. 3d.[43]

5 Second-order nonlinear filamentation instability

Since linear filamentation stability analysis is insufficient to explain late-stage phenomena such as satellite nanowire formation, a nonlinear approach is thus necessary to better understand these behaviors. Fig. 4a illustrates that nonlinear

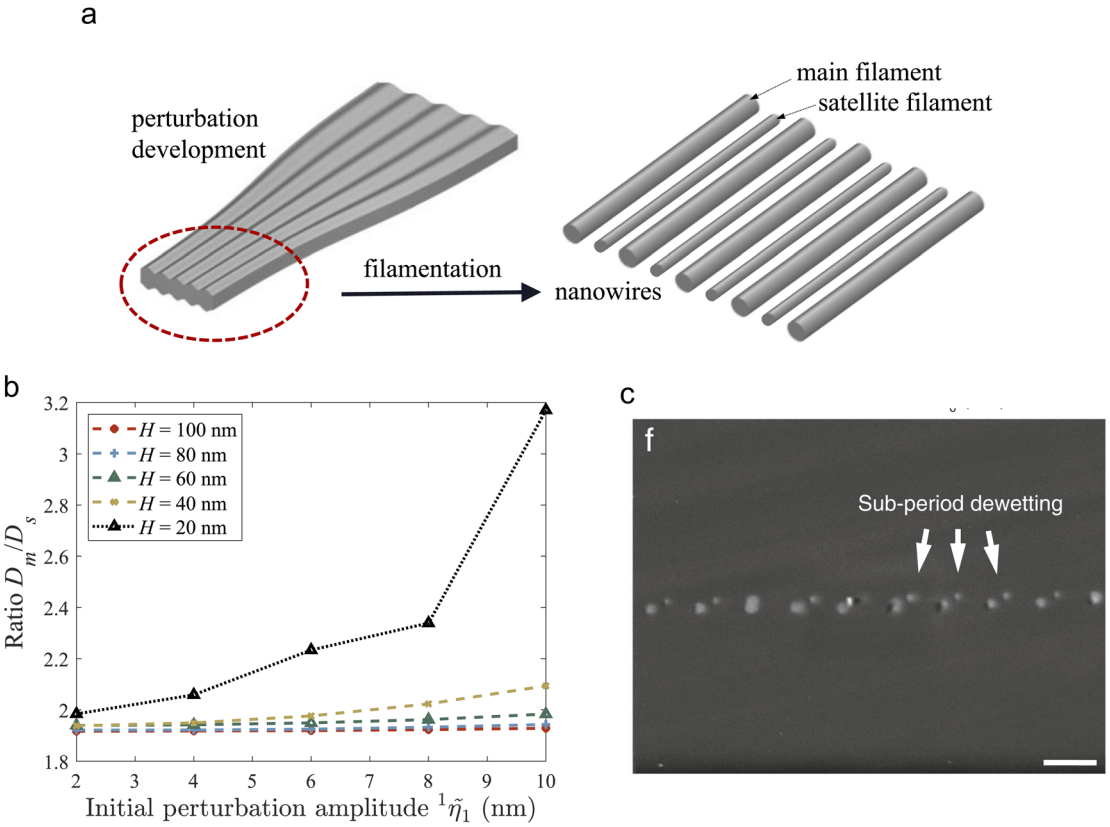

Fig. 4 (a) Schematic diagram of nonlinear filamentation instability resulting in main and satellite nanowires. (b) The influence of liquid sheet thickness and initial perturbation on the diameter ratio between the main filament and the satellite filament. Figures reprinted with permission,[44] copyright (2024) by the American Physical Society. (c) Small satellite nanowires observed in experiments.[43] Figure figure with permission,[43] copyright (2022) by Springer Nature.

filamentation instability will result in main and satellite nanowires. To precisely manipulate filamentation instability and in-fiber nanostructure development, the nonlinear evolution arising from the late stages of the instability was important in previous experiments, where small satellite nanowires could be observed, as shown in Fig. 4c. Moreover, linear filamentation stability analysis focuses on the varicose mode, where the sinuous mode can be neglected. But the harmonic of the sinuous mode presents as a varicose mode in the nonlinear evolution. Thus, it is indispensable to take into account both varicose and sinuous modes in the nonlinear filamentation instability. Second-order nonlinear stability analysis has been performed for 3-layer viscous sheets (a viscous uniform sheet with viscosity μ_1 sandwiched by another viscous fluid with viscosity μ_2), given the coexistence of varicose and sinuous modes. The second-order dispersion relations for varicose and sinuous modes are expressed, respectively, as:[44]

$$\omega_2^{\mathrm{v}} = -k\left(\gamma - \frac{A}{4k^2\pi H^4}\right)$$

$$\frac{\mu_2(\cosh(kH)-1)+\mu_1(\sinh(kH)-kH)}{{\mu_2}^2[\sinh(kH)+kH]+2\mu_1\mu_2\cosh(kH)+{\mu_1}^2[\sinh(kH)-kH]} \quad (6)$$

$$\omega_2^{\mathrm{s}} = -\frac{\gamma_1 k}{2}$$

$$\frac{\mu_2(\cosh(2kH)+1)+\mu_1(\sinh(2kH)+2kH)}{2kH(\mu_1-\mu_2)(\mu_1+\mu_2)+2\mu_1\mu_2\cosh(2kH)+({\mu_1}^2+{\mu_2}^2)\sinh(2kH)} \quad (7)$$

The first-order and second-order contributions to the instability and the influence of the van der Waals force and viscosity have been explored. It is found that second-order perturbations of first-order sinuous and varicose modes are varicose, and the second-order perturbations of the coupled sinuous and varicose modes are sinuous. Moreover, the sinuous first-order perturbations and their varicose second-order ones decay during the instability evolution, as well as the sinuous second-order perturbations of the coupled sinuous and varicose modes. Thus, the varicose first-order perturbations and their varicose second-order perturbations dominate the instability.[44]

Although the stretching effect is not considered, the liquid sheet can be considered to represent the state of the sheet after being stretched. Therefore, the second-order filamentation instability analysis results can provide theoretical predictions for controlling nanowire dimensions and guidance for many fiber applications.[44] Firstly, the satellite nanowire size can be

Table 2 Diameter ratios of main filaments to satellite filaments D_m/D_s. Reprinted with permission,[44] copyright (2024) by the American Physical Society

	The film thickness H/nm				
$1\tilde{\eta}_1$/nm	100	80	60	40	20
2	1.9163	1.9208	1.9390	1.9376	1.9841
4	1.9174	1.9211	1.9414	1.9491	2.0588
6	1.9187	1.9244	1.949	1.9761	2.2339
8	1.9225	1.9320	1.9618	2.0233	2.3393
10	1.9280	1.9427	1.9835	2.0938	3.1701

predicted. These areas on the cross-section can be integrated using the Newton–Raphson method after obtaining the geometric form of the liquid sheet. The cross-sectional area is denoted as A_m for the main filaments, and A_s for the satellite ones. Then, the diameter of the main filaments is estimated *via* $D_m = 2 \times \sqrt{A_m/\pi}$, and the diameter of the satellite filaments *via* $D_s = 2 \times \sqrt{A_s/\pi}$. The diameter ratios of the main filaments to the satellite ones D_m/D_s, in cases with five liquid sheet thicknesses and five different initial perturbation amplitudes $1\tilde{\eta}_1$, are listed in Table 2. The diameter ratio D_m/D_s is maintained between 1.91 and 1.94 at $1\tilde{\eta}_1/H < 0.1$, which means the diameters of the main and satellite filaments are mainly determined by the sheet thickness. As the initial perturbation amplitudes $1\tilde{\eta}_1$ increase, the diameter ratios D_m/D_s increase, and they increase faster under the condition of $1\tilde{\eta}_1/H > 0.1$, as shown in Fig. 4b. Precise prediction of main and satellite nanowire sizes facilitates the production of fibers with self-assembled nanowires.

Moreover, if the sandwiched liquid sheet evolves with complex patterns resulting from nonlinear evolution, but is not yet broken at the cross section, more sophisticated in-fiber nanostructures can be obtained.[44] This implies extensive possibilities for multi-functional fibers with composite nanostructures, thereby presenting intriguing potential applications for nanodevices based on single fibers or integrated fabrics.

6 Conclusion and outlook

In this review, we mainly focus on in-fiber composite nanostructures obtained *via* filamentation instability during thermal drawing. The filamentation instability enables the production of an array of kilometer-long nanowires or a long fiber with self-assembled nanowires. Textured films in the preform with template thickness fluctuation achieve control of the diameter and periodicity of ordered nanowire arrays. The studies on the multilayer and second-order filamentation instability further extend the possibilities of nanowires in a fiber, such as 3D self-assembled nanowires, featuring main nanowires with small satellite nanowires.

Filamentation instability clearly offers more opportunities for deeper research on fluid instability and more sophisticated in-fiber nanostructures. Non-Newtonian fluid properties (such as viscoelastic fluids, shear-thinning fluids and shear-thickening fluids), the dependences of surface tension and viscosity on temperature, more complicated geometries, and so on during thermal drawing are beyond the scope of this review, but may play an important role in filamentation instability. For instance, a targeted investigation into shear-thinning fluids for non-Newtonian fluid systems in filamentation instability is highly actionable, and could clarify how shear-thinning behavior modulates the balance between the stretching effect and van der Waals forces, obtaining diameters of nanowires or nanostructures in fibers different from those in Newtonian fluids. Future work on these factors will facilitate much more precise control of filamentation instability, to fabricate fibers with prescribed nanowires or nanostructures. It is possible that more nanodevices can be realized with multimaterial (such as semiconductors, metals, and polymers) and multifunctional fibers in either single fibers or in large-scale textiles.

Author contributions

B. Xu: conceptualization, writing – original draft, writing – review and editing. P. Li: resources, writing – original draft, writing – review and editing. H. Deng, W. Xia, Q. Meng, W. Yi, Y. Ben: resources, writing – review and editing.

Conflicts of interest

The authors have no conflicts of interest to declare that are relevant to the content of this article.

Data availability

No primary research results, software or code have been included and no new data were generated or analysed as part of this review.

Notes and references

1 G. Loke, W. Yan, T. Khudiyev, G. Noel and Y. Fink, *Adv. Mater.*, 2020, **32**, 1904911.
2 C. Strutynski, R. A. Meza, L. Teulé-Gay, G. El-Dib, A. Poulon-Quintin, J. Salvetat, L. Vellutini, M. Dussauze, T. Cardinal and S. Danto, *Adv. Funct. Mater.*, 2021, **31**, 2011063.
3 Y. Shen, Z. Wang, Z. Wang, J. Wang, X. Yang, X. Zheng, H. Chen, K. Li, L. Wei and T. Zhang, *InfoMat*, 2022, **4**, e12318.
4 X. Chen, Y. Meng, S. Laperrousaz, H. Banerjee, J. Song and F. Sorin, *Natl. Sci. Rev.*, 2024, **11**, nwae290.
5 M. Bayindir, F. Sorin, A. F. Abouraddy, J. Viens, S. D. Hart, J. D. Joannopoulos and Y. Fink, *Nature*, 2004, **431**, 826–829.
6 A. F. Abouraddy, M. Bayindir, G. J. Benoit, S. D. Hart, K. Kuriki, N. D. Orf, O. Shapira, F. Sorin, B. Temelkuran and Y. Fink, *Nat. Mater.*, 2007, **6**, 336–347.
7 F. Sorin, A. F. Abouraddy, N. Orf, O. Shapira, J. Viens, J. Arnold, J. D. Joannopoulos and Y. Fink, *Adv. Mater.*, 2007, **19**, 3872–3877.
8 W. Yan, A. G. Page, T. Nguyendang, Y. Qu, F. Sordo, L. Wei and F. Sorin, *Adv. Mater.*, 2019, **31**, 1802348.

9 H. Banerjee, A. Leber, S. Laperrousaz, R. La Polla, C. Dong, S. Mansour, X. Wan and F. Sorin, *Adv. Mater.*, 2023, **35**, 2212202.
10 Z. Ma, Q. Huang, N. Zhou, Q. Zhuang, S. Ng and Z. Zheng, *Cell Rep. Phys. Sci.*, 2023, **4**, 101300.
11 J. Kim, H. Huang, E. T. Gilbert, K. C. Arndt, D. F. English and X. Jia, *Nat. Commun.*, 2024, **15**, 1686.
12 J. Choi, Q. Zheng, M. E. M. K. Abdelaziz, T. Dysli, D. Bautista-Salinas, A. Leber, S. Jiang, J. Zhang, A. A. Demircali, J. Zhao, Y. Liu, N. W. F. Linton, F. Sorin, X. Jia, E. M. Yeatman, G. Yang and B. Temelkuran, *Adv. Healthcare Mater.*, 2025, 2403235.
13 T. Nguyendang, A. C. de Luca, W. Yan, Y. Qu, A. G. Page, M. Volpi, T. D. Gupta, S. P. Lacour and F. Sorin, *Adv. Funct. Mater.*, 2017, **27**, 1605935.
14 I. Richard, B. Schyrr, S. Aiassa, S. Carrara and F. Sorin, *ACS Appl. Mater. Interfaces*, 2021, **13**, 43356–43363.
15 W. Yan, G. Noel, G. Loke, E. Meiklejohn, T. Khudiyev, J. Marion, G. Rui, J. Lin, J. Cherston, A. Sahasrabudhe, J. Wilbert, I. Wicaksono, R. W. Hoyt, A. Missakian, L. Zhu, C. Ma, J. Joannopoulos and Y. Fink, *Nature*, 2022, **603**, 616–623.
16 A. Sahasrabudhe, L. E. Rupprecht, S. Orguc, T. Khudiyev, T. Tanaka, J. Sands, W. Zhu, A. Tabet, M. Manthey, H. Allen, G. Loke, M. Antonini, D. Rosenfeld, J. Park, I. C. Garwood, W. Yan, F. Niroui, Y. Fink, A. Chandrakasan, D. V. Bohórquez and P. Anikeeva, *Nat. Biotechnol.*, 2024, **42**, 892–904.
17 A. G. Page, M. Bechert, F. Gallaire and F. Sorin, *Appl. Phys. Lett.*, 2019, **115**, 044102.
18 Z. Wang, Z. Wang, D. Li, C. Yang, Q. Zhang, M. Chen, H. Gao and L. Wei, *Nature*, 2024, **626**, 72–78.
19 I. Richard, A. K. Maurya, S. Shadman, E. Masquelier, A. Neels and F. Sorin, *Small*, 2022, **18**, 2101392.
20 F. Gallaire and P.-T. Brun, *Philos. Trans. R. Soc., A*, 2017, **375**, 20160155.
21 F. Schön and M. Bestehorn, *Eur. Phys. J.: Spec. Top.*, 2023, **232**, 375–383.
22 C. Faccini de Lima, L. A. van der Elst, V. N. Koraganji, M. Zheng, M. Gokce Kurtoglu and A. Gumennik, *Nanoscale Res. Lett.*, 2019, **14**, 209.
23 B. Xu, S. Ma, Y. Xiang, J. Zhang, M. Zhu, L. Wei, G. Tao and D. Deng, *Adv. Fiber Mater.*, 2020, **2**, 1.
24 L. van der Elst, C. Faccini de Lima, M. Gokce Kurtoglu, V. N. Koraganji, M. Zheng and A. Gumennik, *Adv. Fiber Mater.*, 2021, **3**, 59–75.
25 J. Zhang, Z. Wang, Z. Wang, T. Zhang and L. Wei, *Nat. Commun.*, 2019, **10**, 5206.
26 Z. Wang, M. Chen, Y. Zheng, J. Zhang, Z. Wang, J. Yang, Q. Zhang, B. He, M. Qi, H. Zhang, K. Li and L. Wei, *Adv. Devices Instrum.*, 2021, **2021**, 9676470.
27 C. Faccini de Lima, F. Wang, T. A. Leffel, T. Miller, S. G. Johnson and A. Gumennik, *Nat. Commun.*, 2023, **14**, 5816.
28 C. Faccini de Lima, T. Leffel, M. Zheng, J. Coulter and A. Gumennik, *Advanced Fabrication Technologies for Micro/Nano Optics and Photonics XVI*, 2023, pp. 34–46.
29 S. Mowlavi, I. Shukla, P.-T. Brun and F. Gallaire, *Phys. Rev. Fluids*, 2019, **4**, 064003.
30 I. Shukla, F. Wang, S. Mowlavi, A. Guyomard, X. Liang, S. G. Johnson and J.-C. Nave, *Phys. Fluids*, 2021, **33**, 122003.
31 D. Deng, N. D. Orf, A. F. Abouraddy, A. M. Stolyarov, J. D. Joannopoulos, H. A. Stone and Y. Fink, *NanoLett.*, 2008, **8**, 4265–4269.
32 D. Deng, J. C. Nave, X. Liang, S. G. Johnson and Y. Fink, *Opt. Express*, 2011, **19**, 16273–16290.
33 R. G. Dorman, *Br. J. Appl. Phys.*, 1952, **3**, 189–192.
34 N. Dombrowski and R. P. Fraser, *Philos. Trans. R. Soc., A*, 1954, **247**, 101–130.
35 H. B. Squire, *Br. J. Appl. Phys.*, 1953, **4**, 167–169.
36 Y. Chao, L. Zhu, Z. Ding, T. Kong, J. Chang and Z. Wang, *Phys. Rev. Fluids*, 2024, **9**, 094001.
37 F. Pino, M. A. Mendez and B. Scheid, *Phys. Rev. Fluids*, 2024, **9**, 104002.
38 J. Stafford, N. Uzo, E. Piccoli, C. Petit and O. K. Matar, *Phys. Rev. Fluids*, 2025, **10**, 024805.
39 A. Oron, S. H. Davis and S. G. Bankoff, *Rev. Mod. Phys.*, 1997, **69**, 931–980.
40 R. V. Craster and O. K. Matar, *Rev. Mod. Phys.*, 2009, **81**, 1131–1198.
41 B. Xu, M. Li, F. Wang, S. G. Johnson, Y. Fink and D. Deng, *Phys. Rev. Fluids*, 2019, **4**, 073902.
42 B. Xu and D. Deng, *Phys. Rev. Fluids*, 2020, **5**, 083904.
43 W. Esposito, L. Martin-Monier, P. L. Piveteau, B. Xu, D. Deng and F. Sorin, *Nat. Commun.*, 2022, **13**, 6154.
44 X. Yang, W. Qiao, H. Deng, Q. Meng, B. Xu and Q. Fu, *Phys. Rev. Fluids*, 2024, **9**, 123902.
45 D. Deng, N. D. Orf, S. Danto, A. F. Abouraddy, J. D. Joannopoulos and Y. Fink, *Appl. Phys. Lett.*, 2010, **96**, 23102.
46 D. Deng, J. Nave, X. Liang, S. G. Johnson and Y. Fink, *Opt. Express*, 2011, **19**, 16273–16290.
47 M. Chen, D. Li, Y. Hou, M. Gu, Q. Zeng, D. Ning, W. Li, X. Zheng, Y. Shao, Z. Wang, J. Xia, C. Yang, L. Wei and H. Gao, *Mater. Horiz.*, 2023, **10**, 5859–5868.
48 M. Chen, J. Xia, J. Zhou, Q. Zeng, K. Li, K. Fujisawa, W. Fu, T. Zhang, J. Zhang, Z. Wang, Z. Wang, X. Jia, M. Terrones, Z. X. Shen, Z. Liu and L. Wei, *ACS Nano*, 2017, **11**, 9191–9199.
49 C. Yang, B. Sun, G. Zhou, T. Guo, C. Ke, Y. Chen, J. Shao, Y. Zhao and H. Wang, *ACS Mater. Lett.*, 2023, **5**, 504–526.
50 P.-G. de Gennes, F. Brochard-wyart and D. Quere, *Capillarity and Wetting Phenomena*, Springer, 2004.
51 A. Javadi, J. Eggers, D. Bonn, M. Habibi and N. M. Ribe, *Phys. Rev. Lett.*, 2013, **110**, 144501.
52 X. Liang, D. Deng, J. C. Nave and S. G. Johnson, *J. Fluid Mech.*, 2011, **683**, 235–262.
53 T. Das Gupta, L. Martin-Monier, W. Yan, A. Le Bris and F. Sorin, *Nat. Nanotechnol.*, 2019, **14**, 320–327.